

Generating Hybrid Interior Structure for 3D Printing

Yuxin Mao^{1†}, Lifang Wu^{1†}, Dong-Ming Yan^{2*}, Jianwei Guo², Chang Wen Chen^{3,4}, Baoquan Chen⁵

¹ College of information and communication engineering, Beijing University of Technology, Beijing, China 100124

² National Laboratory of Pattern Recognition, Institute of Automation, Chinese Academy of Sciences, Beijing, China 100190

³ School of Science and Engineering, Chinese University of Hong Kong, Shenzhen, China 518172

⁴ Department of Computer Science and Engineering, State University of New York at Buffalo, Buffalo, NY 14260-2500, U.S.A.

⁵ Shandong University

† Joint first authors (maoyuxin@emails.bjut.edu.cn; lfwu@bjut.edu.cn). *Corresponding author (yandongming@gmail.com)

Abstract

Generating an interior support structure is a key issue in 3D model geometric optimization for 3D printing. Most existing interior support structures have been designed by simulating lightweight structures naturally exist. One limitation of the existing method is that only one single structure is used for the model. However, different parts of a 3D model have different shapes and mechanical properties and different structures demonstrate distinctive advantages for supporting the model. Based on such observation, we propose to use hybrid structures for designing an optimal support structure. In this paper, we present a novel scheme of generating hybrid interior support structures for 3D printing. The proposed approach first partitions an input model into parts with different physical behaviors. Different interior structures are generated for each part, and the interior structures are finally joined together. Experimental results demonstrate that the proposed hybrid structure obtains higher strength-to-weight ratio than recent competing approaches that use single types of interior structures.

1 Introduction

3D printing techniques have recently become popular due to its powerful ability and flexibility in manufacturing complex 3D shapes. In addition to providing a flexible solution in manufacturing personalized product, 3D printing has also been used in many scientific and industrial applications, e.g., aircraft design, medical structures printing, or even personalized medical support. However, 3D printing also suffers from several practical challenges, such as speed, waste of support material, stability and physical behavior of the printed objects.

One of the most important issues in 3D printing is establishing physically printable and usable prototypes by using less material. The printing material is used in two aspects, one is for the printed object (the shell and infill), and the other is for exterior support structure that must be polished after printing. The material for support structures can be reduced either by selecting better printing orientations or designing smart lightweight support structures. However, the infill structure greatly influences the quality of the printed objects, e.g., strength, stability, and material usage.

Generating infill is a common practice of simulating lightweight structures in nature to obtain high strength-to-weight ratio [31, 16]. Many elegant interior structures have been designed to save materials while retaining the physical properties (see Sec. 2). Existing works focused on designing a single structure inside the volume of the object. However, different structures exhibit distinctive advantages for different stress distributions. For example, the muscle fiber structure has significant directional (anisotropic) stress intensity, whereas the crystal structure has uniform (isotropic) stress intensity in all directions. Filling an isotropic space with fiber structure might cause significant material waste. In this work, we propose to use different structures in regions with different stress behaviors.

In our approach, an input 3D model is first partitioned into different components based on their shape and stress distribution. A part of shape can be classified as anisotropic and isotropic with respect to their physical behavior. An anisotropic region always exhibits column-like (Col) structure, whereas an isotropic region has non-column (NCol) structure. The Col components are further validated through mechanical analysis. The components that passed the validation are further classified as valid Col (VCol) structure. Therefore, we focused on these two types of components. One is VCol component with high stress in the axial direction and the other is NCol component. The interior support structure of the VCol component is generated using the *muscle fiber structure* (MFS), whereas its NCol component is formed using the *tetrahedral crystal structure* (TCS). Furthermore, transient structures are generated at the interface between the components. These structures are designed to preserve the connection between neighboring components.

The contribution of our work is two-fold. First, we demonstrated that hybrid interior support structures are suitable for various 3D models in 3D printing. We also developed a strategy to partition the 3D model to match different structures with specific shape and mechanical properties. Second, we designed two specific structures, MFS and TCS, to generate hybrid structures in 3D models that can be partitioned into Col and NCol components. We also designed transient layers for connecting MFS and TCS to generate a complete hybrid interior support structure for a 3D model.

2 Related Work

Many works have been conducted on different stages of 3D printing pipeline [14]. The major challenges of 3D printing techniques include the issues in efficiency, strength, material usage, and physical behavior of the printed objects [4]. In this section, we briefly discuss the representative works and then emphasize on the problem of interior structure design with the aim of using less material while retaining the strength of the printed objects. More comprehensive discussion can be found in the recent survey papers [13, 27].

To print large objects, several approaches addressed the problem of decomposing the input models into printable parts [8, 17, 9, 5, 24, 10]. To enhance the physical strength, Stava et al. [25] and Zhou et al. [44] proposed to thicken the weakest part of the model. Umetani and Schmidt [26] optimized the printing process by analyzing the stress of cross sections. Wang et al. [28] optimized the structure by considering the force from any direction instead of only one direction. The efficiency of the printing

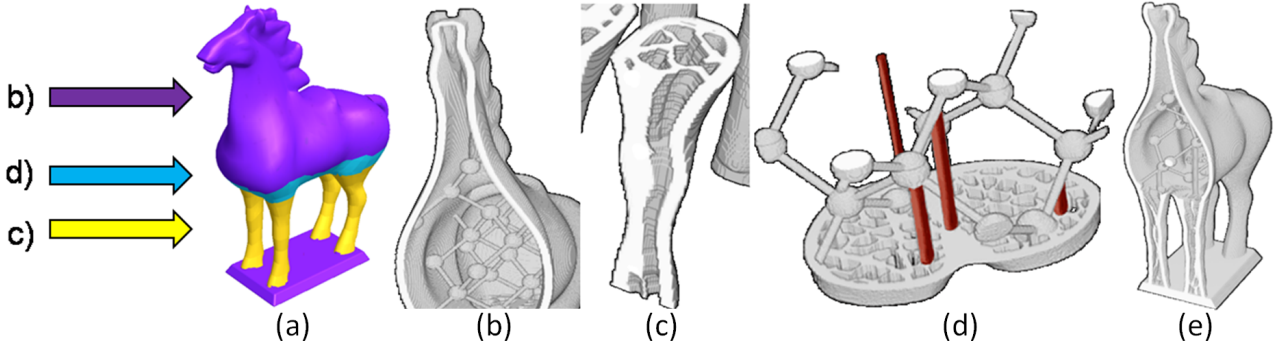


Figure 1: Proposed MFS-TCS scheme. (a) Model partition. (b) Generating interior support structure for NCol components. (c) Generating interior support structure for VCol components. (d) Generating the transient structures. (e) Cut-view of the final result.

process can also be improved by optimizing the slices [29, 2]. Other works focus on the function of the printed object, for example, standing ability [20], rotatability [3], or floatation [38].

One of the most important issues in 3D printing is the reduction of printing materials for both infill and exterior support structure. Dumas et al. [11] introduced the well-known scaffold structure from building construction to 3D printing to reduce support material in fused filament fabrication. Zhang et al. [42] reduced the support material by optimizing the printing directions. Reiner and Lefebvre [21] proposed an interactive system for support-free printing. Wu et al. [32] used a robot arm to control the print process of segmented 3D shapes, whereas each component can be printed on top of the printed parts in a support-free direction. Several recent works focus on designing support-free interior structures for 3D printing [41, 37]. In the most recent work, Wang et al. [30] proposed a hollowing framework that can fabricate voids inside a solid, instead of using any interior support structure.

Inspired from various porous structures in nature (e.g., beehive, rhombic, trabecular bone, etc...), which exhibit excellent stability and high strength-to-stress ratio, many approaches are proposed to mimic such structures for infill design [12]. Martínez et al [18] simulated randomized Voronoi foams in printing micro structures using procedural modeling. This type of approach can be regarded as an extension of 2D texture synthesis technique. Wang et al. [31] examined the frame structure used in buildings and proposed a skin-frame structure in which the interior was composed of steel structure of the building and the exterior was wrapped by the surface skin. A tradeoff can be achieved between the cost of printing materials and model strength. Lu et al. [16] proposed an internal optimized support structure with multiple holes produced by a clipped Voronoi diagram [39]. Zhang et al. [43] used medial axis for interior support, while Wu et al [36] proposed to use an adaptive rhombic structure for infill design. In their recent work, Wu et al. [34] designed bone-like infill structure based on topology optimization technique [35, 33]. However, using a single type of interior structure might still cause material wasting, or weaken the strength in thin regions. Inspired by the work of Stave et al. [25], we present a hybrid structure to further improve the strength-to-weight ratio.

3 Overview

Our system consists of three main components, i.e., model partition, stress analysis, and interior structure generation, as illustrated in Fig. 1. First, the input shape is roughly segmented into isotropic and anisotropic regions according to the *shape diameter function* (SDF) [22] (Sec. 4), as shown in Fig. 1(a). If the SDF value is smaller than a threshold, then the corresponding part is classified as a candidate Col component (anisotropic), otherwise, NCol component (isotropic). We aim to keep the components as large as possible, because generating a large number of interior structures using too many small components is time-consuming. Then, each component of the partitioned model is classified into VCol and NCol component by applying mechanical analysis on the model (Sec. 4.2). Next, the interior support structures are generated for different components (Sec. 5). The MFS is used for VCol components, and the TCS is used for NCol components. Finally, the boundaries of interior components are blended with transient structures (Sec. 6).

4 Model Partition

In this step, an input shape is partitioned into several components according to their shape. Each component is then verified by mechanical analysis.

4.1 Partition with SDF

The SDF [22] is a scalar function defined on the mesh surface. SDF expresses the diameter of the object’s volume in the neighborhood of each point on the surface and is efficient to differentiate Col and NCol structures. If we consider a point on the input surface mesh and take the normal vector as the center line for drawing a cone, then we could draw lines within the model starting at the vertex and finishing on the mesh and calculate the weighted average values for all the lines. This average is the SDF value. The normalized SDF $nsdf(f)$ of a facet f is defined as follows:

$$nsdf(f) = \frac{\log\left(\frac{sdf(f) - \min(sdf)}{\max(sdf) - \min(sdf)} \cdot \alpha + 1\right)}{\log(\alpha + 1)},$$

where $sdf(f)$ is the SDF for each facet f ; α is a normalization parameter, which is set to 4 in all our experiments. If $nsdf(f)$ is smaller than the threshold, then $nsdf(f)$ is considered as a candidate Col component, otherwise, NCol component. We set this threshold to 0.26 experimentally. Fig. 2(a-top) shows an example of model partition. The horse model is partitioned into six components: one NCol component (the body) and five Col components (four legs and the tail).

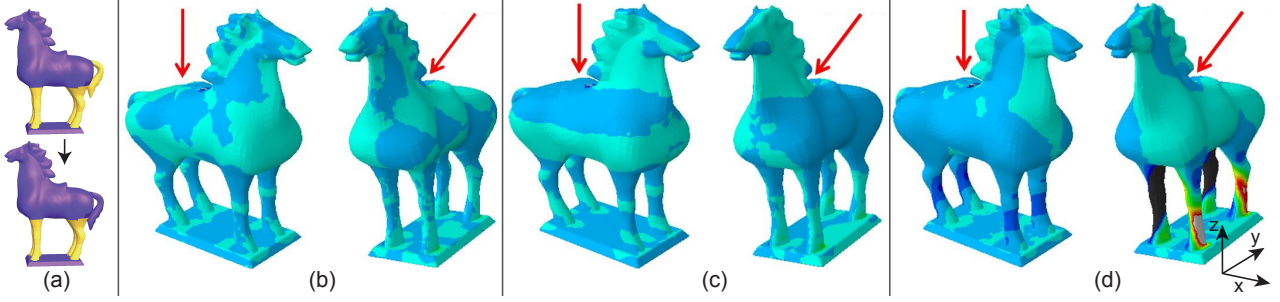


Figure 2: (a) Partition (top) and verification (bottom) of the horse model. (b, c, and d) Stress in three directions with forces from two directions applied to the horse model. In the left-hand column, the force is exerted from the top. In the right column, the force is exerted from top-right at the same point (the angle is 45 degree between the X-axis and the Z-axis). The red arrows indicate the force directions.

4.2 Component verification

In this step, we analyze the stress of each candidate component and classify them into VCol and NCol. A 1000N force is applied on the model as shown in Fig. 2. The corresponding stress distributions in three directions (x, y, and z) are shown in Fig. 2. The average stress in each component is computed and used to verify the component types. If no dominant stress in three directions exists, the component is classified as NCol, otherwise as VCol. If two neighboring components are NCol, then they will be merged into one component, e.g., the tail and the body of the horse model as shown in Fig. 2(a-bottom).

5 Interior Structure Generation

Once the input shape is partitioned and the components are classified, we can generate interior support structures for VCol and NCol components.

5.1 Muscle Fiber Structure for VCol Components

The shape of VCol is column-like and the dominant stress is in the axial direction. The strength in the axial direction is much higher than those in radial and tangential directions, similar to a multiple cylindrical like structure [6] muscle fiber. This property coincides with the requirement of the VCol components. Therefore, to generate interior support structure is reasonable for VCol components by simulating the muscle fiber structure, which can be generated by extruding the 2D porous structure in the axial direction. In our implementation, the VCol component is cut into slices perpendicular to the axial direction using parallel planes. We first generate a 2D MFS for each sectional plane, and the final MFS can be obtained by connecting neighboring 2D MFSs.

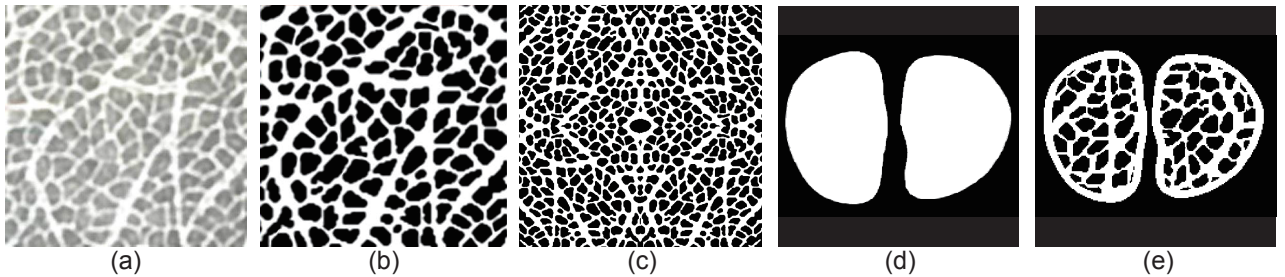


Figure 3: Preprocessing of the intersection image of skeletal muscle. (a) Input muscle fiber texture. (b) Binarization. (c) Synthesized higher resolution image. (d) Mask of the sectional plane of VCol component. (e) Sectional result of MFS.

From the template image of muscle fiber, as shown in Fig. 3(a), we convert into a binary image using the watershed algorithm Fig. 3(b). The white pixels in Fig. 3(b) represent the support part and the black pixels correspond to the voids. The size of the image could be adjusted to fit the size of the sectional plane Figure 3(c). Finally, the slice and the binary image are joined by AND operation. The interior structure for a single slice is generated as shown in Fig. 3(e). The slices of interior structures are connected using the Marching Cubes [15] algorithm. Fig. 4(a) shows two examples of MFS generated by our algorithm.

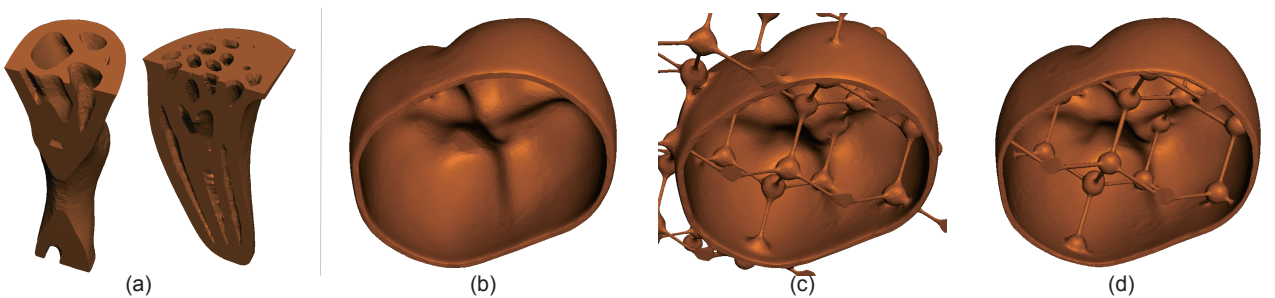


Figure 4: (a) MFSs of the front left leg of the horse and the front left root of the tooth model. (b) Cut-view of a NCol component. (c) Overlaid with TCS. (d) Interior TCS generated by boolean operation.

5.2 Tetrahedral Crystal Structure for NCol Components

The NCol components have no dominant stress direction, and should afford loads in all directions. Therefore, we choose the TCS for interior support design, because the TCS has high uniform strength in any direction. For example, the ultrahard materials in nature such as diamond and some precious stones have such structures [1].

The TCS can be easily generated inside NCol components by 3D Boolean operation [7]. Given a NCol component and a TCS in 3D space, the part inside the NCol component is clipped and kept as the interior support structure, see Fig. 4(d). Several parameters are available that can be tuned for TCS generation, i.e., resolution of TCS, size of balls and sticks. A common observation is that the resolution of TCS, corresponds to the strength of the printed objects; and the size of balls and sticks corresponds to the strength. While increasing the strength, more material would be used. Balancing the strength and material usage depends on the downstream applications.

6 Transient Structure Generation

The transient structure is designed to connect the neighboring components. For practical application, the following criterion should be met: 1) The material should be consumed as less as possible. 2) The neighboring components should be connected. 3) The strength of the model should be preserved. By the above criterions, the transient structures are generated by two steps. The first step is to generate the transient layer, which is the intersection volume whose two sides are intersected with the neighboring components. The next step is to generate the extended support columns for supporting the TCS structure, so that the strength on the TCS side could be preserved.

6.1 Generating the Transient Layer



Figure 5: Intersection plane of the transient layer. (a) Normal position and Reverse position. (b) Illustration of the region connection. (c) The intersection of the transient layer.

Since MFS and TCS are generated separately in previous steps, we have to add an additional transient layer to connect the interior of the neighboring components. Generally, we assume that the neighboring components are MFS and TCS structures. Two intersecting planes could be represented as binary images $S_{MFS}(x, y)$ and $S_{TCS}(x, y)$, as shown in Fig. 5(a). The white region should be supported in the corresponding components. While the black means not a support point. The union $US(x, y)$ of two binary images could be obtained as follows:

$$US(x, y) = S_{MFS}(x, y) \cup S_{TCS}(x, y).$$

Ideally, $US(x, y)$ includes only one connected region with value 1. If more than one regions exist, as shown in Fig. 5(b), the regions should be connected. We suppose that M regions exist with value 1, R_i^1 , $i=1, 2, \dots, M$ and N regions with value 0, R_j^0 , $j=1, 2, \dots, N$. The largest globally connected region is represented as R_1^1 . Other regions are the small regions, which are encompassed in one of the regions with value 0. Hence, no support is available for them. They should be connected to region R_1^1 . For a small region R_i^1 , we first find the corresponding R_j^0 and obtain the bounding box of R_i^1 , which is represented as $B_{Left}B_{Right}B_{Top}B_{Bottom}$. $US(x, y)$ could be modified in following way.

Example of the connected regions is shown in Fig. 5(b). In this region, the pixels of blue color should be hollowed, while the pixels in the orange color should be preserved. For example, the transient layer for the tooth model is shown in Fig. 5(c). Only six support points exist (two dominant points and four secondary points, marked in red color) to the TCS structure on the transient layer, which means that the stress of the TCS structure will be concentrated on the six points. It is possibly overloaded and this part of the model is fragile. Therefore the extended structures are needed to support the TCS structures.

6.2 Generating extended support columns

To disperse the stress of the TCS, we augment the extended support columns in transient regions. Using criterion 1 specified in the beginning of Sec. 6, we should introduce as less as additional support points in the transient layer, i.e., the extended transient structure should be added to the existing support region on the transient layer.

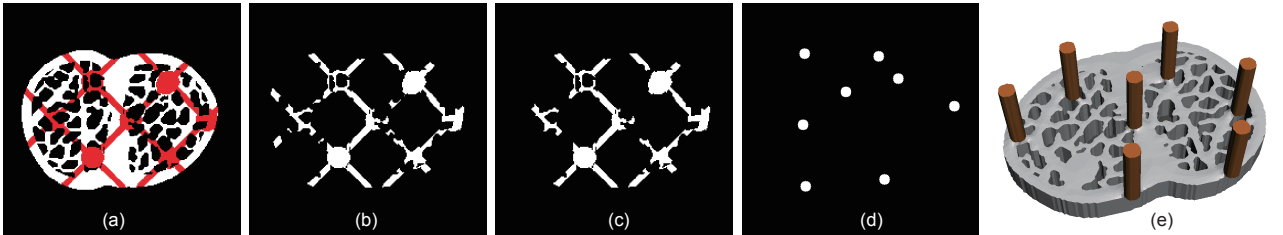


Figure 6: Illustration of generating extended support columns. (a) Projection of TCS structure. (b) Results of the AND operation. (c) After removing small regions. (d) Support points sampling. (e) Extended support columns.

Fig. 6 illustrates this procedure. First, the TCS is projected on the transient layer (Figure 6(a)). Then AND operation is applied between the projection of TCS and the transient layer(Fig. 6(b)). Next, the regions in Fig. 6(b) are clustered and the small regions are discarded, as shown in Fig. 6(c). Furthermore, support points are sampled using the Poisson-disk sampling algorithm [40] (Fig. 6(d)). Finally, extended support columns are augmented at the support points in vertical direction, as shown in Fig. 6(e). Their support bars could share the stress from TCS, which help to increase the strength of the final model. The effectiveness of the transient layer is demonstrated in Fig. 10 in the results section.

7 Experimental Results

In this section, we first present several interior support structures generated by proposed algorithm and conduct mechanical testing by fabricating the results then squeezing using a mechanical device. Next, we analyze the behavior of our approach with varying parameters, e.g., different resolution and shifting of TCS. Finally, we compare our results with representative state-of-the-art technique that uses single type of interior structures, in term of the strength and material usage.

Analysis and evaluation. Fig. 7 shows interior support structures of two examples by slicing the resulting models. Different structures are generated for different parts in these models. The transient layers, such as the 250th layer of the tooth model and the 310th layer of the horse model, connect the MFS and TCS structures and preserve the connection between two components.

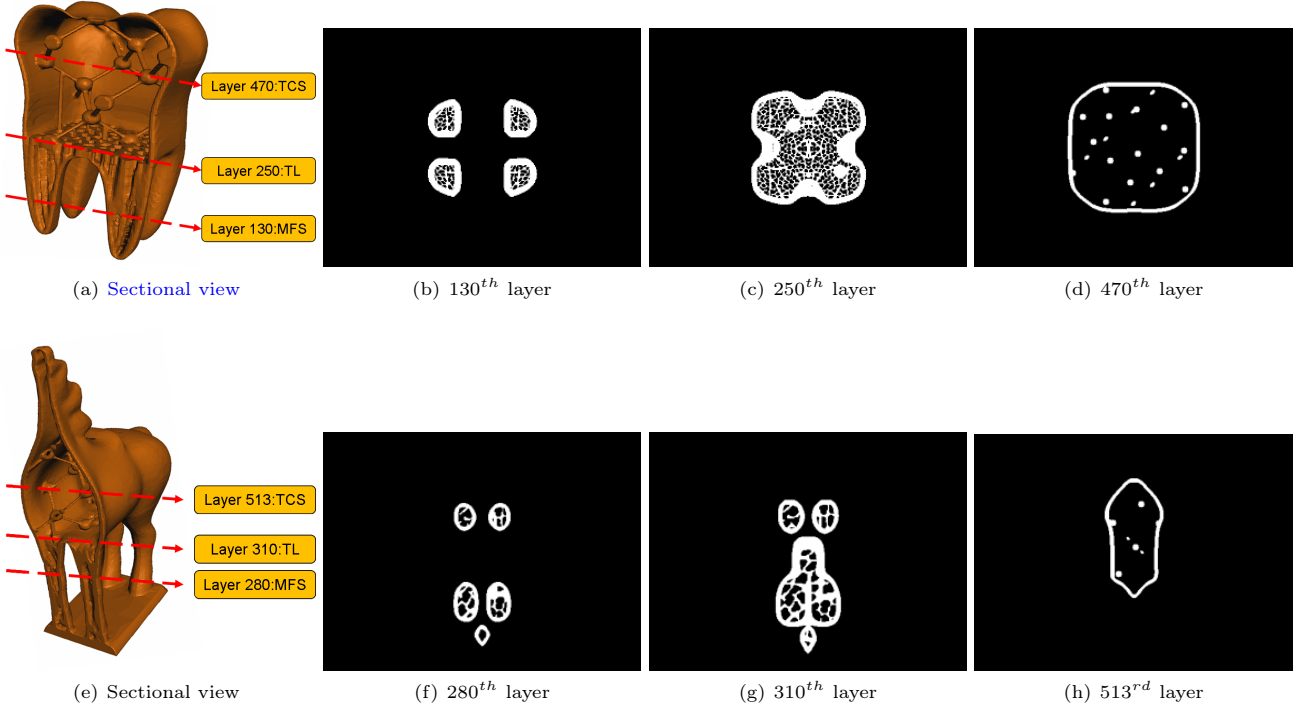


Figure 7: Interior support structure for tooth (top) and horse (bottom) models.

Next, we analyze the properties using only MFS or TCS, and the combined structure by fabricating the corresponding results. As shown in Fig. 8, the size of the bounding box is 8cm, 5cm, and 4cm for all the printed objects. The weights of stored materials are 5g, 8g and 13g for the models with TCS, MFS-TCS, and MFS respectively. The TCS model and the MFS-TCS model are interior connected as shown in Fig. 8(a) and Fig. 8(c), respectively. The printed objects with the proposed algorithm are heavier than that with only the TCS model but lighter than that with MFS model. This is reasonable because the proposed algorithm is the combination of MFS and TCS. The weight of the proposed model is about 41.86% of the solid model.



Figure 8: Printed objects with different interior support structure and their weights. (a) Model with only TCS. (b) Models with only MFS. (c) Models with hybrid MFS-TCS. (d) Solid model.

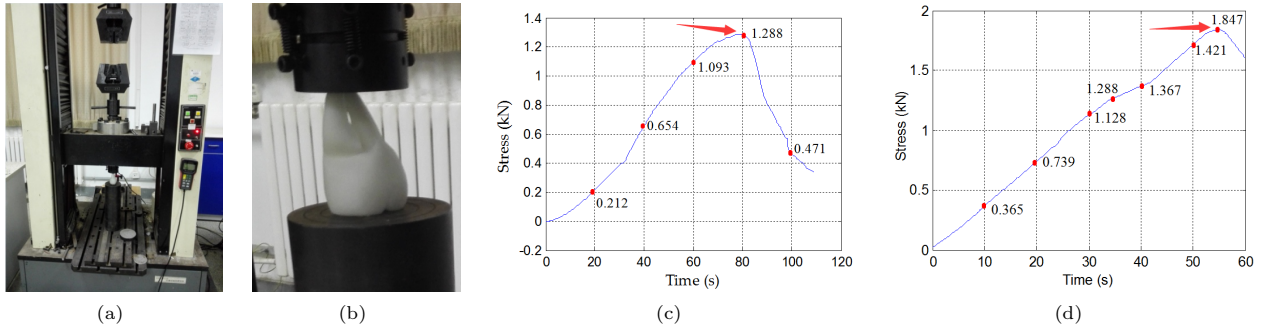


Figure 9: Mechanical testing device (a) and the zoom-in view (b). Stress change curves for the model with TCS (c) and the proposed model (d).

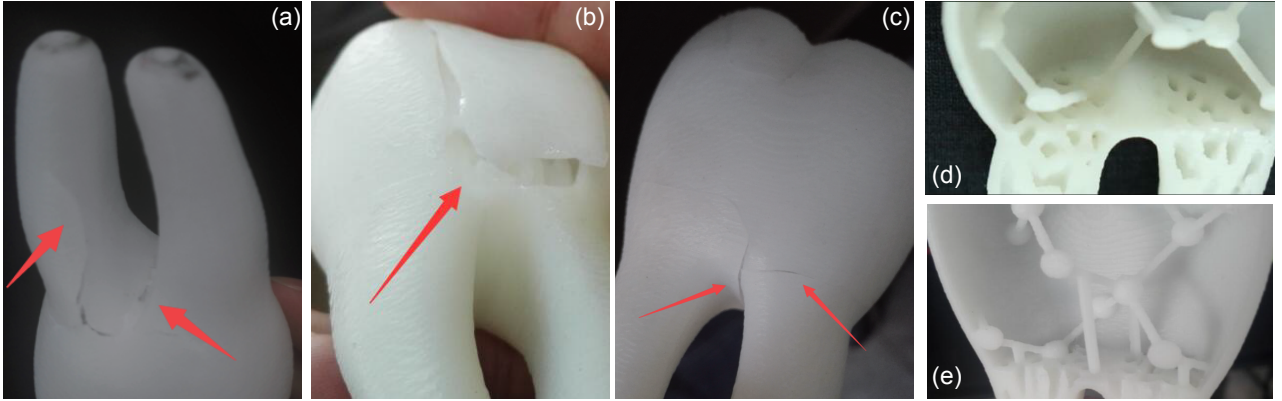


Figure 10: Left: the breaking state of the printed objects. (a) Model of TCS. (b) Model of MFS-TCS without transient structure. (c) Model with transient layer. Right: details of the transient structure for the MFS-TCS model. (d) Cut-view of MFS-TCS without the transient layer. (e) Cut-view of the transient structure, including the transient layer and the extended support columns.

We conducted mechanical testing on the printed objects to verify the strength of different support structures. The testing device is shown in Fig. 9(a) and Fig. 9(b). The object is placed on the platform. Then the force is applied to the objects and increased gradually. The stress variation is recorded. The test is stopped when the object starts to break. The recorded stress variation curves are shown in Fig. 9(c) and Fig. 9(d). The maximum force that the TCS model could bear is 1.288kN, whereas that of the MFS-TCS model is 1.847kN.

The breaking state of each model are shown in Fig. 10(a to c). We observed that the connections between the tooth root and the tooth crown are broken first. However, in Fig. 10(b), the MFS-TCS model is broken at the tooth crown with the TCS structure, not the transient part. Meaning the transient structure is stronger. We could further increase the strength of the object by increasing the strength of the TCS structure. Although the extended support columns could form more support points to the TCS in Fig. 10(d), however, additional supports are not available in the model with transient layers as shown in Fig. 10(e).

Influence of resolution and shift. We use TCS to fill NCol regions, which is a structure consists of balls and sticks. The strength of this structure is related to resolution and thickness of the sticks. We conducted two experiments to verify the effectiveness of this structure. First, we analyze the behavior of the TCS under shift transformation for isotropic regions. Since TCS is shift invariant in 3D space, which is the same as our scenario, we shifted the TCS in four directions of the monkey model, as shown in Fig. 11. The total volumes of the four results are approximately the same and do not differ from those in the strength analysis. Next, we analyze the strength of the TCS structure using different resolutions and different thickness of the sticks. We conclude that if too few balls and sticks in the structure, then the strength will not be isotropically strong enough. Thicker sticks indicate stronger strength, but more material usage. Finding the relationship among resolution, thickness, and strength is work of future work.

Comparison. We conduct physical comparison of our approach and several representative state-of-the-art approaches, including Voronoi hollowing [16], bone-like porous structure [34], and rhombic infill structure [36]. The cut-views of all these results are shown in Fig. 12. To conduct the mechanical simulation, we first normalize all the models to the same scale $51.8mm \times 46.7mm \times 78.5mm$, and generate tetrahedral meshes using open-source software TetGen [23]. Then, we apply 110N force on top of each model, and simulate their physical behavior using the open source library OOFEM [19]. The corresponding simulation result of each model is shown on the right side. It is shown that our result can sustain similar force as others while keeping unbroken, but with less material usage.

8 Conclusion

In this paper, we presented a new approach of generating hybrid interior support structure for 3D printing model. We first demonstrated that a hybrid interior support structure is suitable for various 3D models in 3D printing. We then designed a scheme to partition the model into VCol and NCol components and generate different interior support structures for different components. We used MFS and TCS for VCol and NCol components with preserved strength. The effectiveness and the physical properties of our results are verified through mechanical simulation and comparison with previous works.

Some limitations are not addressed in current approach. For example, the segmentation is based on SDF, which is not directly related to the physical behavior of the objects to be printed. The transient layer works in simple shapes but might have problems when multiple parts are connected. Our system cannot print large object either. In the future, we would like to address these

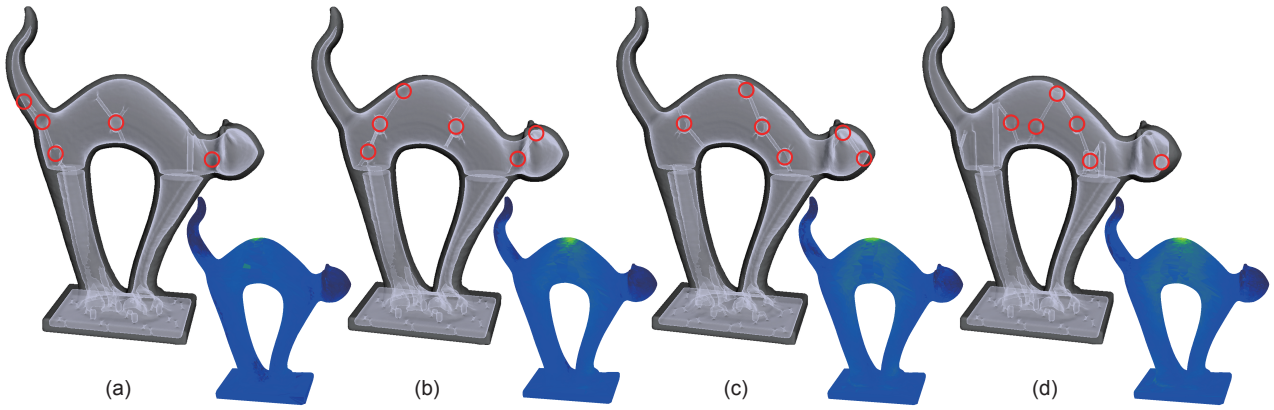


Figure 11: Effectiveness of the TCS under shift transformation. From left to right are the results of shift up, down, left and right. The number of balls and sticks are 5 balls and 8 sticks; 6 balls and 7 sticks; 6 balls and 7 sticks; 6 balls and 10 sticks, respectively. The total volume of each result are $5539.3cm^3$, $5447.0cm^3$, $5454.1cm^3$, and $5447.0cm^3$. The simulation results are shown on the right side.

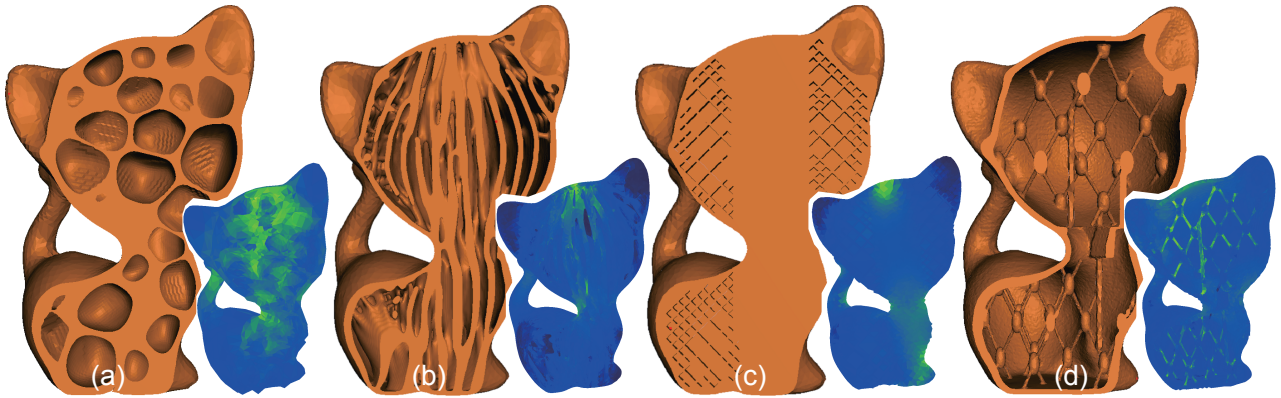


Figure 12: Comparison with other approaches: (a) Voronoi hollowing [16] (46.02 gram), (b) bone-like porous structure [34] (52.74 gram), (c) rhombic infill structure [36] (78.82 gram), and (d) ours (31.53 gram). For the simulation results, the coolness of color corresponds to the stress.

limitations. We also plan to investigate new interior support structures that consist of multiple types of primitives and complement the physical property of complicated 3D objects.

Acknowledgements

We thank anonymous reviewers for their insightful and constructive suggestions. We also thank Dr. Jun Wu for providing us with their results for comparison. This project was partially supported by the National Natural Science Foundation of China (Nos. 61772523, 61372168 and 61620106003), Beijing Municipal Education Commission Science and Technology Innovation Project (KZ201610005012), and Beijing Natural Science Foundation (4184102).

References

- [1] *Diamond Structure*. Springer Berlin Heidelberg, 2009.
- [2] M. Alexa, K. Hildebrand, and S. Lefebvre. Optimal discrete slicing. *ACM Trans. Graph.*, 36(1):12:1–12:16, 2017.
- [3] M. Bäcker, E. Whiting, B. Bickel, and O. Sorkine-Hornung. Spin-It: Optimizing moment of inertia for spinnable objects. *ACM Trans. on Graphics (Proc. SIGGRAPH)*, 33(4):96:1–96:10, 2014.
- [4] B. Bickel, M. Bäcker, M. A. Otaduy, H. R. Lee, H. Pfister, M. Gross, and W. Matusik. Design and fabrication of materials with desired deformation behavior. *ACM Transactions on Graphics*, 29(4):1–10, 2010.
- [5] X. Chen, H. Zhang, J. Lin, R. Hu, L. Lu, Q. Huang, B. Benes, D. Cohen-Or, and B. Chen. Dapper: decompose-and-pack for 3D printing. *ACM Trans. on Graphics (Proc. SIGGRAPH Asia)*, 34(6):213:1–213:12, 2015.
- [6] E. L. Fox, R. W. Bowers, and M. L. Foss. *The physiological basis for exercise and sport*. WM. C. BROWN PUBLISHERS, 1993.
- [7] M. Granados, P. Hachenberger, S. Hert, L. Kettner, K. Mehlhorn, and M. Seel. Boolean operations on 3D selective nef complexes: Data structure, algorithms, and implementation. *Lecture Notes in Computer Science*, 9(5):833–855, 2003.
- [8] R. T. Haftka and R. V. Grandhi. *Structural shape optimization a survey*. Elsevier Sequoia S. A., 1986.
- [9] R. Hu, H. Li, H. Zhang, and D. Cohen-Or. Approximate pyramidal shape decomposition. *ACM Trans. on Graphics (Proc. SIGGRAPH Asia)*, 33(6):213:1–213:12, 2014.
- [10] A. K. Jadoon, C. Wu, Y.-J. Liu, Y. He, and C. C. Wang. Interactive partitioning of 3D models into printable parts. *IEEE Computer Graphics and Applications*, 2017. accepted.
- [11] S. L. Jérémie Dumas, Jean Hergel. Bridging the gap: Automated steady scaffoldings for 3D printing. *ACM Trans. on Graphics (Proc. SIGGRAPH)*, 34(4), 2014.

- [12] J. Kindinger. Lightweight structural cores. *ASM Handbook*, 21:180–183, 2001.
- [13] L. Liu, C. Wang, A. Shamir, and E. Whiting. 3D printing oriented design: Geometry and optimization. In *Siggraph Asia Course*, 2014.
- [14] M. Livesu, S. Ellero, J. Martínez, S. Lefebvre, and M. Attene. From 3D models to 3D prints: an overview of the processing pipeline. *Computer Graphics Forum*, 36(2):537–564, 2017.
- [15] W. E. Lorensen and H. E. Cline. Marching cubes: A high resolution 3D surface construction algorithm. *ACM Siggraph Computer Graphics*, 21(4):163–169, 1987.
- [16] L. Lu, A. Sharf, H. Zhao, Y. Wei, Q. Fan, X. Chen, Y. Savoye, C. Tu, D. Cohen-Or, and B. Chen. Build-to-last: strength to weight 3D printed objects. *ACM Trans. on Graphics (Proc. SIGGRAPH)*, 33(4):97, 2014.
- [17] L. Luo, I. Baran, S. Rusinkiewicz, and W. Matusik. Chopper: Partitioning models into 3D-printable parts. *ACM Trans. on Graphics (Proc. SIGGRAPH Asia)*, 31(6):129:1–129:9, 2012.
- [18] J. Martínez, J. Dumas, and S. Lefebvre. Procedural Voronoi foams for additive manufacturing. *ACM Trans. on Graphics (Proc. SIGGRAPH)*, 35(4):44:1–44:12, 2016.
- [19] B. Patzák and D. Rypl. Object-oriented, parallel finite element framework with dynamic load balancing. *Advances in Engineering Software*, 47(1):35–50, 2012.
- [20] R. Prévost, E. Whiting, S. Lefebvre, and O. Sorkine-Hornung. Make It Stand: Balancing shapes for 3D fabrication. *ACM Trans. on Graphics (Proc. SIGGRAPH)*, 32(4):81:1–81:10, 2013.
- [21] T. Reiner and S. Lefebvre. Interactive modeling of support-free shapes for fabrication. In *Eurographics (short papers)*, pages 25–28, 2016.
- [22] L. Shapira, A. Shamir, and D. Cohen-Or. Consistent mesh partitioning and skeletonisation using the shape diameter function. *The Visual Computer*, 24(4):249–259, 2008.
- [23] H. Si. Tetgen, a Delaunay-based quality tetrahedral mesh generator. *ACM Trans. Math. Softw.*, 41(2):11:1–11:36, Feb. 2015.
- [24] P. Song, B. Deng, Z. Wang, Z. Dong, W. Li, C.-W. Fu, and L. Liu. Cofifab: Coarse-to-fine fabrication of large 3D objects. *ACM Transactions on Graphics (Proc. Siggraph)*, 35(4):45:1–45:11, 2016.
- [25] O. Stava, J. Vanek, B. Benes, and N. Carr. Stress relief: improving structural strength of 3D printable objects. *ACM Trans. on Graphics (Proc. SIGGRAPH)*, 31(4):48:1–48:11, 2012.
- [26] N. Umetani and R. Schmidt. Cross-sectional structural analysis for 3d printing optimization. In *SIGGRAPH Asia 2013, Technical Briefs*, pages 5:1–5:4, 2013.
- [27] C. C. L. Wang and Y. Chen. Geometric and physical modeling for additive manufacturing. *Computer-Aided Design*, 69:63–64, 2015.
- [28] T. Y. Wang, Y. Liu, X. Liu, Z. Yang, D.-M. Yan, and L. Liu. Global stiffness structural optimization for 3D printing under unknown loads. *Journal of Computer Graphics Techniques*, 5(3):18–38, 2016.
- [29] W. Wang, H. Chao, J. Tong, Z. Yang, X. Tong, H. Li, X. Liu, and L. Liu. Saliency-preserving slicing optimization for effective 3D printing. *Comput. Graph. Forum*, 34(6):148–160, 2015.
- [30] W. Wang, Y. J. Liu, J. Wu, S. Tian, C. C. L. Wang, L. Liu, and X. Liu. Support-free hollowing. *IEEE Trans. on Vis. and Comp. Graphics*, 2017. accepted.
- [31] W. Wang, T. Y. Wang, Z. Yang, L. Liu, X. Tong, W. Tong, J. Deng, F. Chen, and X. Liu. Cost-effective printing of 3D objects with skin-frame structures. *ACM Trans. on Graphics (Proc. SIGGRAPH Asia)*, 32(6):177, 2013.
- [32] C. Wu, C. Dai, G. Fang, Y. Liu, and C. C. L. Wang. Robofdm: A robotic system for support-free fabrication using FDM. In *IEEE International Conference on Robotics and Automation, ICRA*, pages 1175–1180, 2017.
- [33] J. Wu, N. Aage, S. Lefebvre, and C. C.-L. Wang. Topology optimization for computational fabrication. In *Eurographics 2017 – Tutorials*, 2017.
- [34] J. Wu, N. Aage, R. Westermann, and O. Sigmund. Infill optimization for additive manufacturing – approaching bone-like porous structures. *IEEE Trans. on Vis. and Comp. Graphics*, 2017. accepted.
- [35] J. Wu, C. Dick, and R. Westermann. A system for high-resolution topology optimization. *IEEE Trans. on Vis. and Comp. Graphics*, 22(3):1195–1208, 2016.
- [36] J. Wu, C. C. L. Wang, X. Zhang, and R. Westermann. Self-supporting rhombic infill structures for additive manufacturing. *Computer-Aided Design*, 80:32–42, 2016.
- [37] Y. Xie and X. Chen. Support-free interior carving for 3D printing. *Visual Informatics*, 1(1):9–15, 2017.
- [38] Y. Xie, Y. Yuan, X. Chen, C. Zheng, and K. Zhou. Continuous optimization of interior carving in 3d fabrication. *Frontiers of Computer Science*, 11(2):332–346, 2017.
- [39] D.-M. Yan, W. Wang, B. Lévy, and Y. Liu. Efficient computation of clipped Voronoi diagram for mesh generation. *Computer-Aided Design*, 45(4):843–852, 2013.
- [40] D.-M. Yan and P. Wonka. Gap processing for adaptive maximal Poisson-disk sampling. *ACM Trans. on Graphics*, 32(5):148:1–148:15, 2013.
- [41] Y. Yang, S. Chai, and X.-M. Fu. Computing interior support-free structure via hollow-to-fill construction. *Computers & Graphics*, 70:148 – 156, 2018.
- [42] X. Zhang, X. Le, A. Panotopoulou, E. Whiting, and C. C. L. Wang. Perceptual models of preference in 3D printing direction. *ACM Trans. Graph.*, 34(6):215:1–215:12, 2015.
- [43] X. Zhang, Y. Xia, J. Wang, Z. Yang, C. Tu, and W. Wang. Medial axis tree – an internal supporting structure for 3D printing. *Computer Aided Geometric Design*, 35–36:149–162, 2015.
- [44] Q. Zhou, J. Panetta, and D. Zorin. Worst-case structural analysis. *ACM Transactions on Graphics*, 32(4):1–12, 2013.